# Supporting Information

# Electric field-induced assembly in single-stacking terphenyl junctions

Yongxiang Tang‡, Yu Zhou‡, Dahai Zhou‡, Yaorong Chen, Zongyuan Xiao, Jia Shi, Junyang Liu, Wenjing Hong*

State Key Laboratory of Physical Chemistry of Solid Surfaces, *i*ChEM, NEL, College of Chemistry and Chemical Engineering, Xiamen University, Xiamen 361005, China.

**Section 1. Synthesis and experiments**



**Section 2. Supporting conductance measurements**

**Section 1. Synthesis and experiments**

1. Synthesis of the compounds

1,4-bis((4-(methylthio)phenyl)ethynyl)benzene (**S2**) and 4,4''-bis(methylthio)-1,1':4',1''-terphenyl (**S1**) were purchased from Sigma-Aldrich.

(2',3',5',6'-tetramethyl-[1,1':4',1''-terphenyl]-4,4''-diyl) bis (methylsulfane) (**S3**) and 9,10-bis(4-(methylthio)phenyl) anthracene were prepared according to previous report.[1] **S3** and 9,10-bis(4-(methylthio)phenyl) anthracene were synthesized via Suzuki cross coupling reactions of 1,4-diiodo 2,3,5,6-tetramethylbenzene, 9,10-dibromoanthracene with 4-(methylthio) phenylboronic acid.

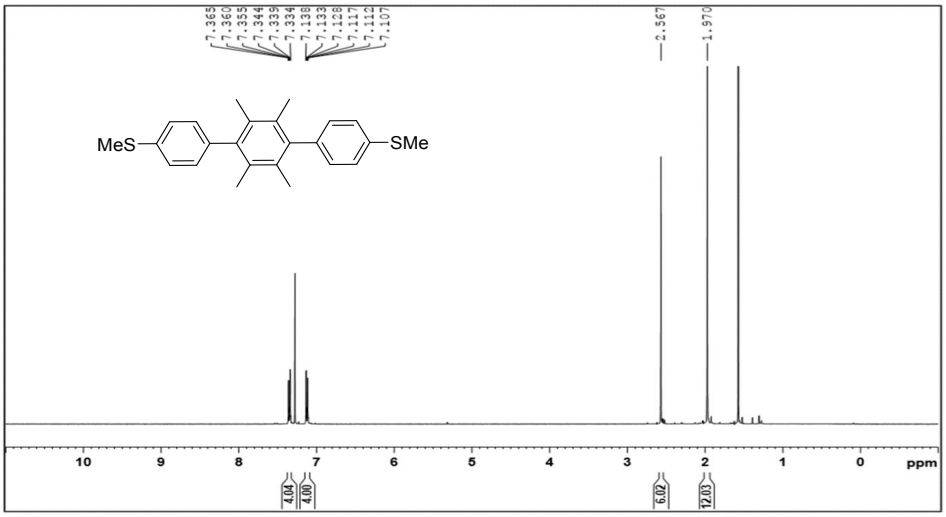


**Figure S1**. $^{1}$HNMR (400 MHz, $CDCl_3$) of **S3**.

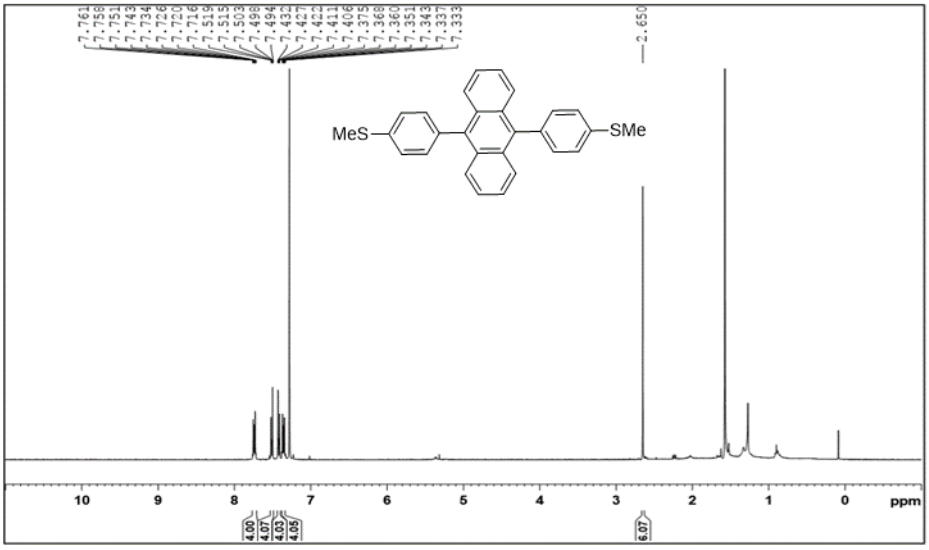


**Figure S2**. $^{1}$HNMR (400 MHz, $CDCl_3$) of **9,10-bis(4-(methylthio)phenyl)anthracene**.

4,4'-bis(methylthio)-1,1'-biphenyl (**S4**) is synthesized as follows.

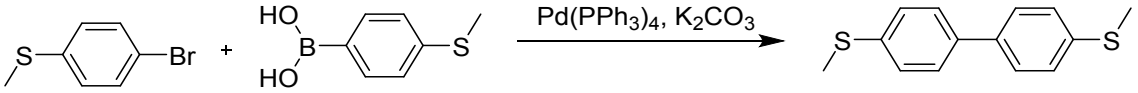


4-Bromothioanisole (609 mg, 3 mmol), 4-(Methylthio)phenylboronic acid (756 mg, 4.5 mmol), Pd(PPh3)4 (173 mg, 0.15 mmol) and K2CO3 (1.24 g, 9 mmol) was placed into a 250 mL two-necked round bottom flask . The flask was evacuated under vacuum and flushed with dry nitrogen three times and then 80 mL mixture of methylbenzene, ethyl alcohol, and water (3/1/1, v/v/v) was added. The reaction mixture was refluxed for 6 h. After cooling to room temperature, the mixture was poured into water and extracted with dichloromethane three times. The combined organic layers were dried over anhydrous magnesium sulfate. After filtration and solvent evaporation, the crude product was purified by silica-gel column chromatography.

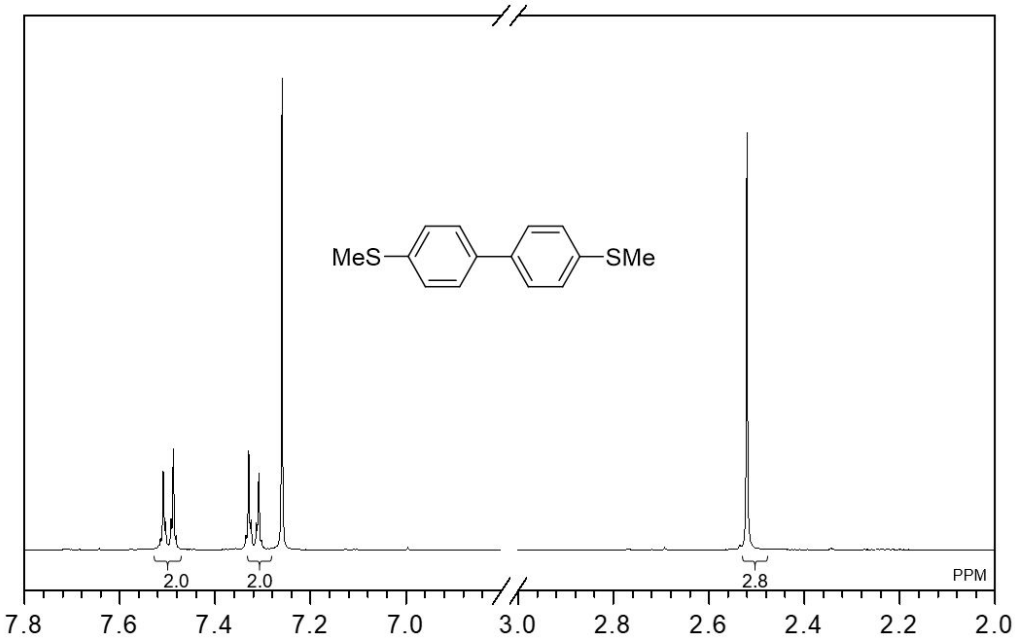


**Figure S3**. [1]HNMR (400 MHz) of **S4**. [1]H NMR (400 MHz, $CDCl_3$), $\delta$ (ppm): 7.52 - 7.46 (m, 2H), 7.35 - 7.29 (m, 2H), 2.52 (s, 3H).

4,4''-diamine -1,1':4',1''-terphenyl (**N1**), benzidine (**N2**) and 9H-fluorene-2,7-diamine were purchased from Sigma-Aldrich.

[1,1':4',1'':4'',1''':4''',1''''-quinquephenyl]-4,4''''-diamine (N3) was prepared according to previous report.2 4,4'-Dibromoterphenyl, 4-(N-Boc-amino) phenylboronic acid pinacol ester, cesium fluoride, tetrakis (triphenylphosphine) palladium(0) were mixed and reacted in a pressure vessel with a Teflon screw-cap and protected with nitrogen. After adding anhydrous THF, the vessel was sealed and stirred at 80 °C for 16 h. The mixture was cooled to room temperature, and the resulting solid was collected by filtration. The solid was washed with water and THF, then suspended in dichloromethane and cooled to 0 °C to which trifluoroacetic acid was added. The reaction was warmed to room temperature and stirred for 16 h. The reaction was filtered and basified by the addition of NaOH in water. The resulting solid was washed with dichloromethane, water, and acetone to give the desired product as an off-white solid.

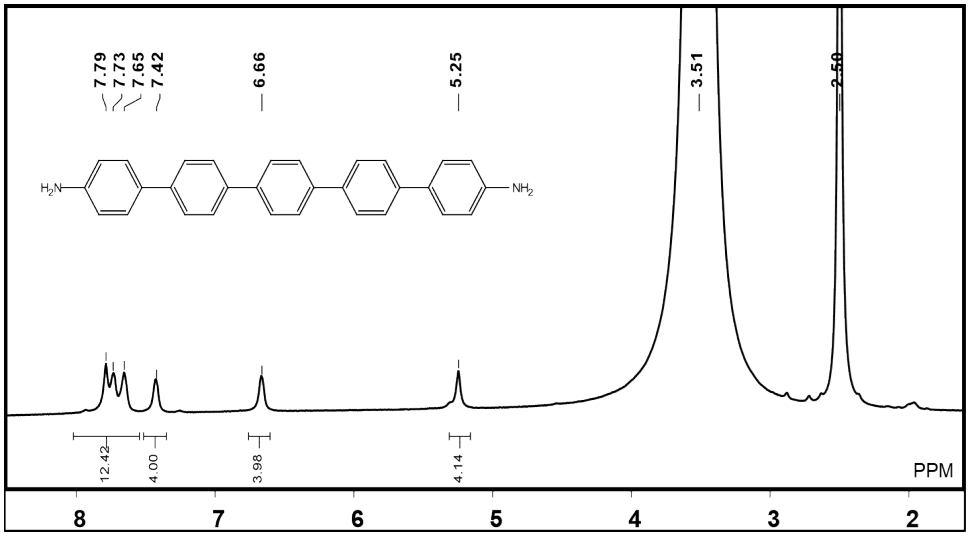


**Figure S4**. 1HNMR (500 MHz, d6-DMSO) of **N3**.

## 2. Experimental procedures

Preparation for the experiments: Gold wire (99.99%, 0.25 mm diameter) was purchased from Beijing Jiaming Platinum Nonferrous Metal Co, Ltd. for the fabrication of the STM tip. The gold tip is cleaned by flame to form a gold bead. Substrates were prepared by depositing a 100 nm thick gold film on the N<111> monocrystalline face of a silicon wafer. The gold-coated substrate was cleaned by immersed in piranha solution (V ($H_2SO_4$): V($H_2O_2$) = 3:1 CAUTION! piranha solution is extremely corrosive) for about 4 hours and was rinsed with fresh deionized water for 5 minutes. After this time, the substrate was moved into fresh deionized water, and the boiling procedure repeated for a total of three cycles.[2] Then, the substrate can be used after drying.

The sample preparation: The target molecules were mixed with TMB and THF (THF:TMB = 1:4) into a solution with a concentration of 0.1 mM.

**Figure S5**. The photos of home-built STM setup.

## Section 2. Supporting Conductance Measurements

### The break-junction experiments of molecule S1

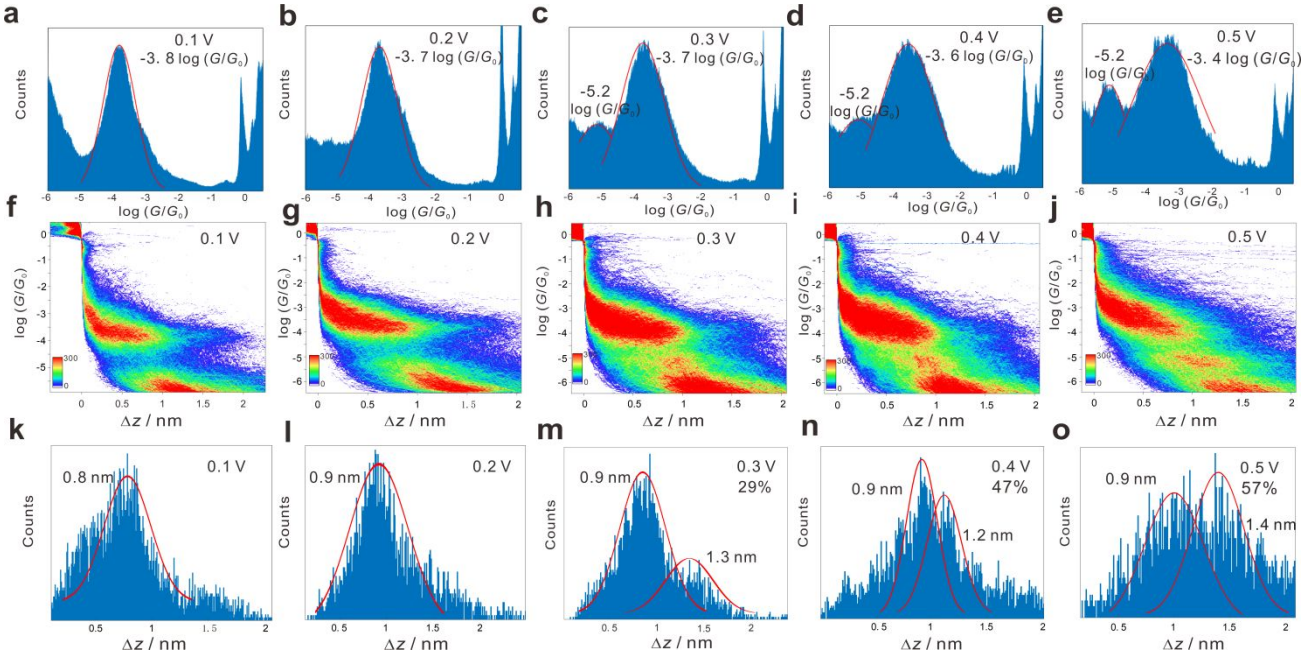


**Figure S6**. Break-junction experiments of **S1** under different biases and length distribution analysis. a-e, 1D conductance histograms of **S1** from 0.1 V to 0.5 V. f-j, 2D conductance histograms of **S1** from 0.1 V to 0.5 V. k-o, length distribution analysis of **S1** under different biases with a bimodal distribution from monomer and dimer, respectively, the percentage shows the ratio of the distribution of dimer.

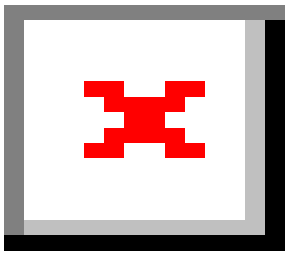

**Figure S7**. 2D conductance histogram of **S1** of closing process under 0.35 V.

We study the conductance under low bias voltage with 0.01 V and 0.05 V. The results show that a smaller bias voltage would lead to a smaller conductance range, making it difficult to measure the stacking process (Figure S8).

**Figure S8**. Break-junction experiments of **S1** under low bias voltage.

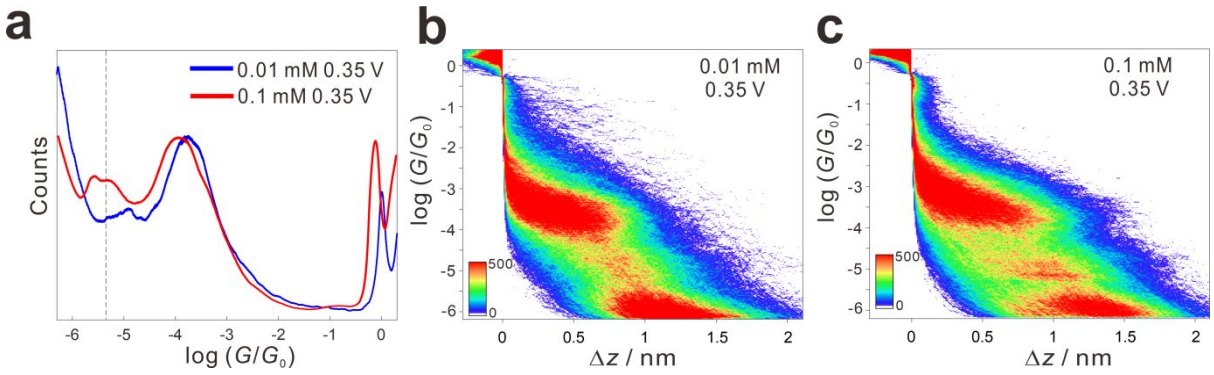


**Figure S9.** Break-junction experiments of **S1** with variable concentration. a, 1D conductance histograms, and typical conductance-displacement traces of **S1** under 0.35 V with 0.01 mM (blue) and 0.01 mM (red). b-c, 2D conductance histogram of S1 under 0.35 V with 0.01 mM (b) and 0.1 mM (c).

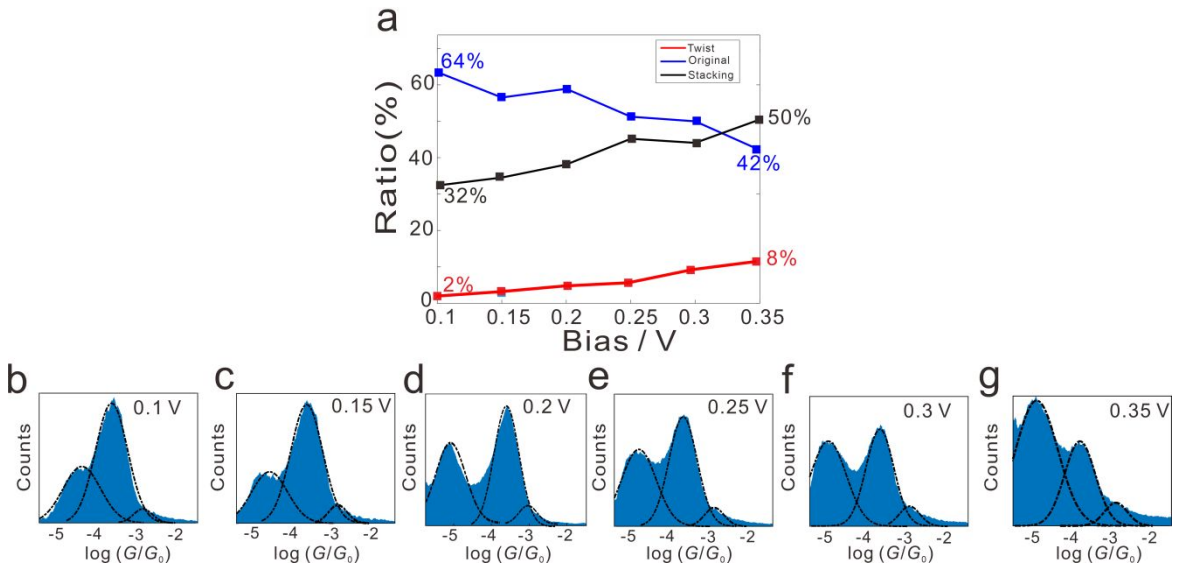


**Figure S10**. Statistical analysis of conductance plateaus of **S1** for suspending tips traces, the methods are shown in Section 2. a, The ratio of three conductance peaks from counting the plateau and integral peak area in Figure 1. b-e, The 1D conductance plateau histogram, through counting the plateaus in each traces from suspending tips.

**The break-junction experiments of control molecules**

To study the electric field-induced stacking of shorter/longer oligophenyl junctions, we analyzed the conductance of shorter oligophenyl junctions of **S4** and longer oligophenyl junctions of **N2** under different bias voltage. **S4** shows a more apparent low conductance under high bias voltage, which is considered to be the conductance of the stacking junction. Meanwhile, the high-conductance increases under high bias voltage (Figure S11b), which indicates that the higher conductance structure with a low twist angle is captured. Therefore, we suggest that although the effect of electric field-induced stacking of **S4** is not significant compared with that of **S1** because the coupling between the electrode and **S4** would impede the molecular deformation more than the coupling between the electrode and **S1**, it still exists in **S4**. While **N2** shows a more apparent low conductance under high bias voltage. However, the length of the low-conductance structure is more consistent with the coupling according to previous study (Figure S11d).[3] As for the longer oligophenyl **N3**, because of its long molecular length, the middle benzene ring of **N3** may be coupled with the gold electrode by the Au-π interaction,[4] which leads to a high conductance due to the reduction of the charge transfer distance. Intrinsic conductance of **N3** is around $10^{-5.0}$ $G_0$ (Figure S11g), and the signal of the dimer is expected to be ~ $10^{-7.0}$ $G_0$, which is too low to be detected by our device, and we also do not observe the twist signal for the higher conductance. Therefore, longer oligophenyl junctions do not find similar trends that twist angle reduces that promotes the stacking process.

To sum up, the effect of electric field-induced stacking still exists in shorter oligophenyl junctions. However, due to the current limit of instrumental measurement, the conductance signal originated from stacking effect in longer oligophenyl molecules is difficult to be captured.

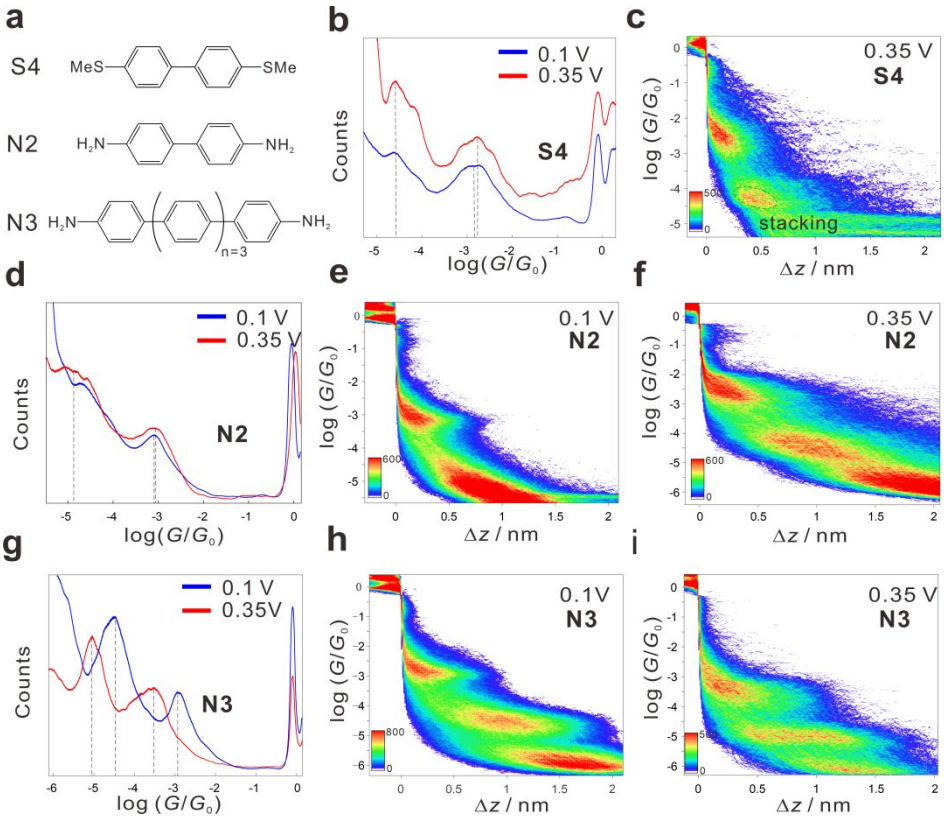


**Figure S11**. Break-junction experiments on oligophenyl junctions of different lengths. a, Structures of the molecules. b, 1D conductance histograms of **S4** under 0.1 V(blue) and 0.35 V(red). c, 2D conductance histograms of **S4** under 0.35 V. d, 1D conductance histograms of **N2** under 0.1 V (blue) and 0.35 V (red). e-f, 2D conductance histograms of **N2** under 0.1 V (e) and 0.35 V (f). g, 1D

conductance histograms of quinquephenyl under 0.1 V(blue) and 0.35 V (red). h-i, 2D conductance histograms of **N3** under 0.1 V (h) and 0.35 V (i).

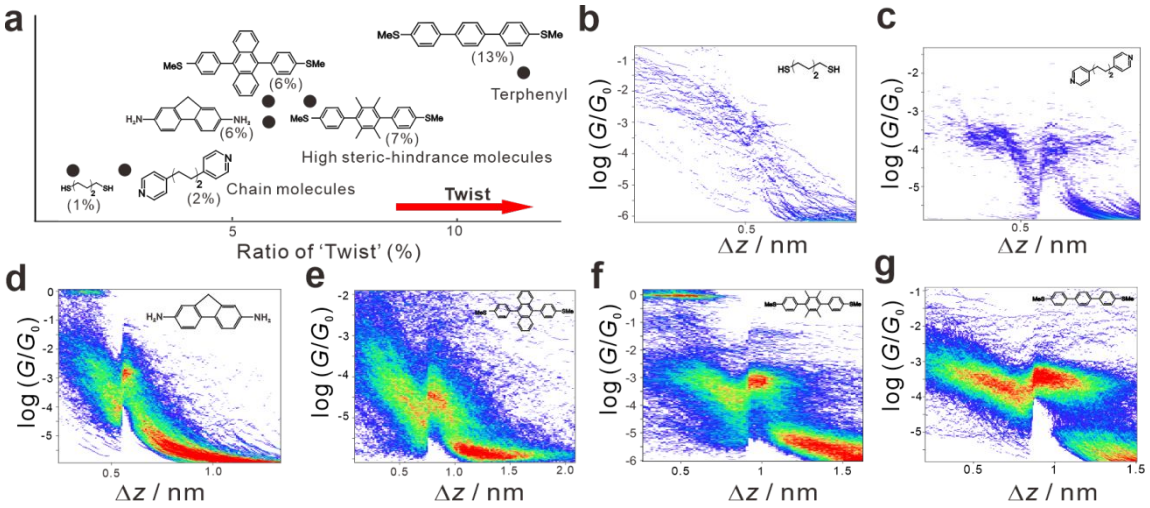


**Figure S12**. 2D conductance histogram of traces with twist features. a, ratio of 'twist' like traces of several molecules compared with terphenyl. b-c, the 2D histogram of the traces with 'twist' features of the chain molecules under 0.10 V. d-f, the 2D histogram of the traces with 'twist' features of the high steric-hindrance molecules under 0.10 V. g, the 2D histogram of the traces with 'twist' features of the **S1** under 0.10 V.

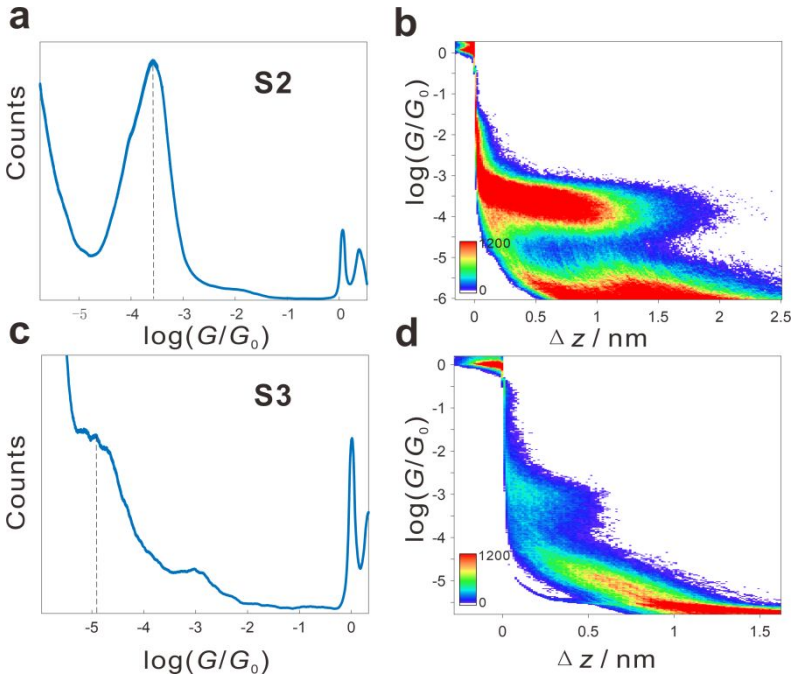


**Figure S13**. 1D and 2D conductance histogram of **S2** and **S3**. a, 1D conductance histogram of **S2** under 0.10 V. b, 2D conductance histogram of **S2** under 0.10 V. d, 1D conductance histogram of **S3** under 0.10 V. e-f, 2D conductance histogram of **S3** under 0.10 V.

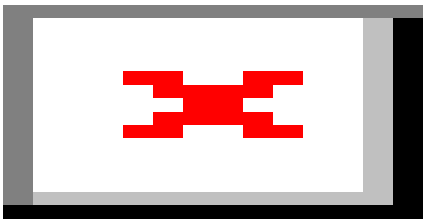

**Figure S14**. Solvent experiments. a, 1D conductance histogram of pure solvent TMB, inset is typical break-junction traces, the conductance plateaus are marked by a red stripe. b, typical traces of **S1** and **N1**, the conductance plateaus from the solvent are marked by a red stripe.

**The supporting results of I-V analysis**

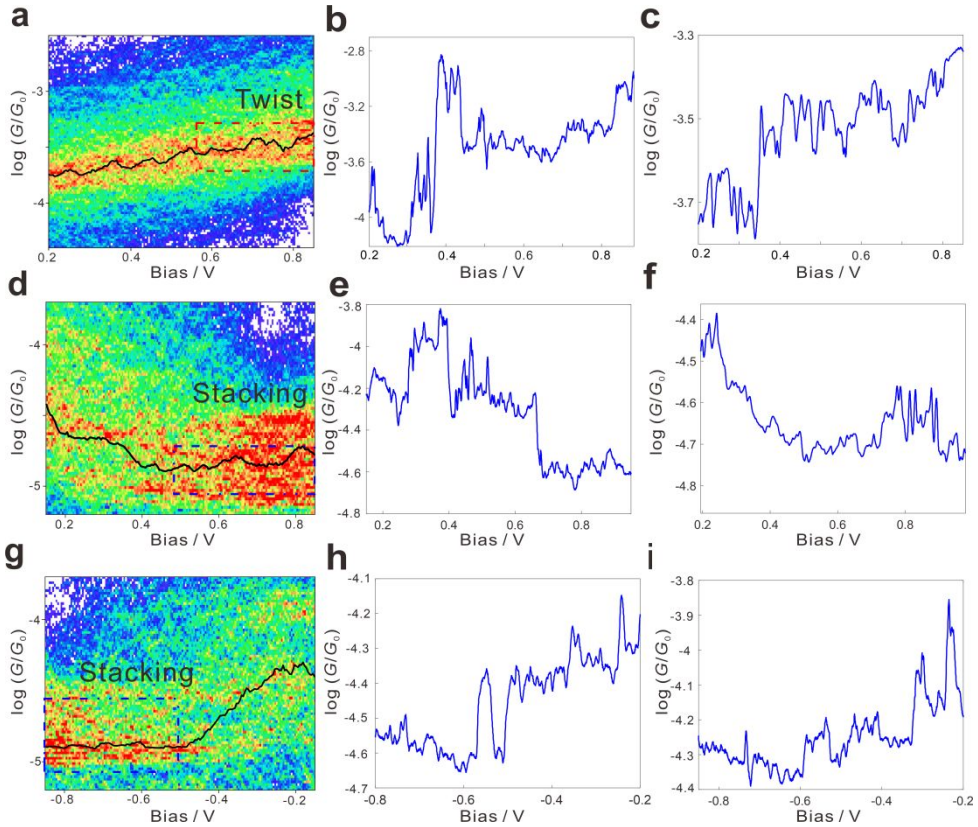


**Figure S15**. Results of conductance-voltage measurements of **S1**. a-c, 2D dimensional histogram (a) and typical traces (b-c) of *I-V* scan of **S1** with the conductance region in [$10^{-3.0}$ $G_0$, $10^{-4.0}$ $G_0$]. d-f, 2D dimensional histogram (d) and typical traces (e-f) of *I-V* scan of **S1** with the conductance region in [$10^{-4.0}$ $G_0$, $10^{-5.0}$ $G_0$]. g-i, 2D dimensional histogram (g) and Typical traces of opposite *I-V* scan with the conductance region in [$10^{-4.0}$ $G_0$, $10^{-5.0}$ $G_0$] (h-i). The 'twist' and 'stacking' conductance states under high bias voltage marked by a red and blue box, respectively.

**The supporting results of noise analysis**

Previous studies found that high-frequency fluctuations occur during dimer formation,[5] Therefore, we have analyzed the conductance noise of terphenyl break-junction data and added it to the Supporting Information. We added Figure S16 to discuss the fluctuation in Supporting Information. We used conductance noise analysis to extract the high-frequency noise in low conductance.[6] As is shown in Figure S16, although the low conductance shows a little higher variation than that of high conductance, however, the difference is not apparent, and it is much smaller than the fluctuation of two orders of magnitude reported in the literature of ref. 6. We think that oscillation in previous studies is difficult to be clearly captured with our instruments. The source of the oscillations is from the DQI produced by alternating HOMO-LUMO orbital overlap. The micromachining chip they used provides sufficient stability (attenuation coefficient is generally in the order of $10^{-5}$), so the distance resolution of the electrode stretching is high enough to distinguish one benzene ring and one triple bond. Thus the oscillation from the sliding of positive and negative on the HOMO orbital can be observed during the pulling process. However, limited by the current instrument, we can't keep the stretching under that slow rate to get such oscillation with fluctuation of two orders of magnitude. Therefore, this case may occur with molecule **S1**, but we can't clearly capture it under the instrumental condition.

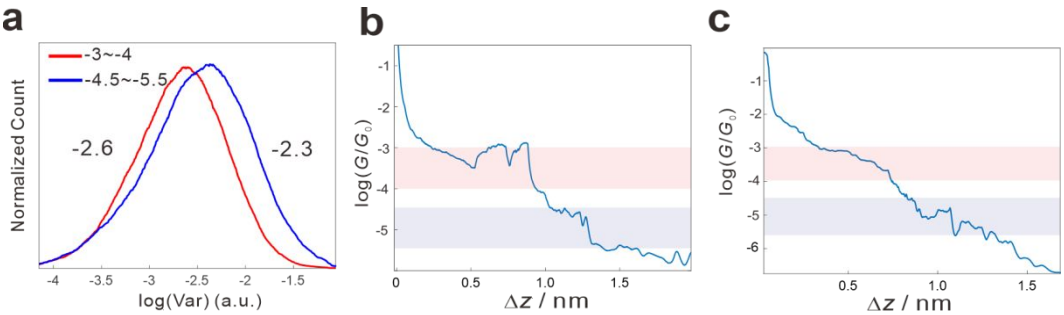


**Figure S16**. Fluctuation analysis of break-junction data. a, Conductance noise distribution of **S1** under 0.50 V. b-c, Typical traces of break-junction traces of **S1**, the regions counted are marked by the rectangle.

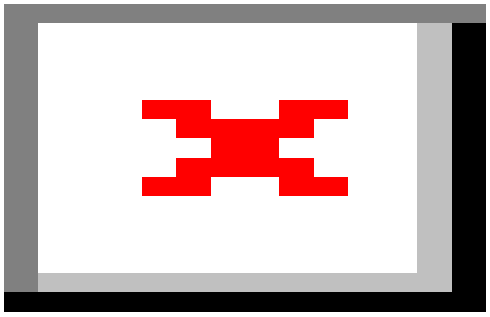

**Figure S17**. Flicker noise distribution of **S1** under different biases from 0.10 V to 0.35 V.

**The supporting results of correlation analysis**

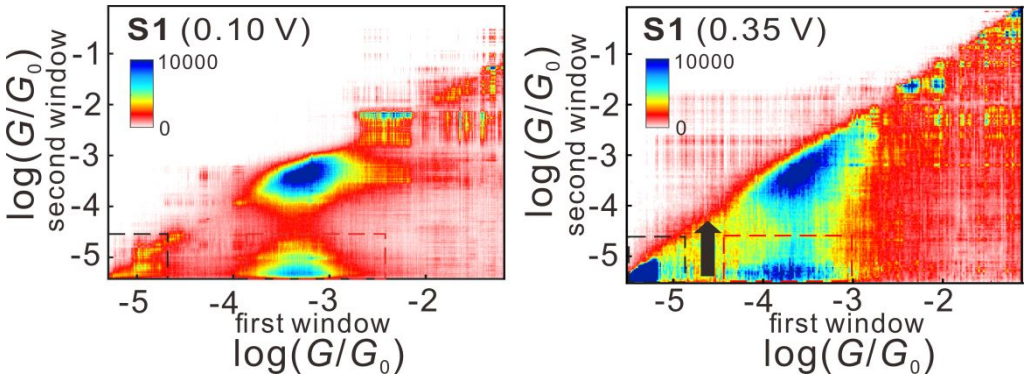


**Figure S18**. Correlation histogram of the sliding box on **S1** under 0.10 V and 0.35 V.

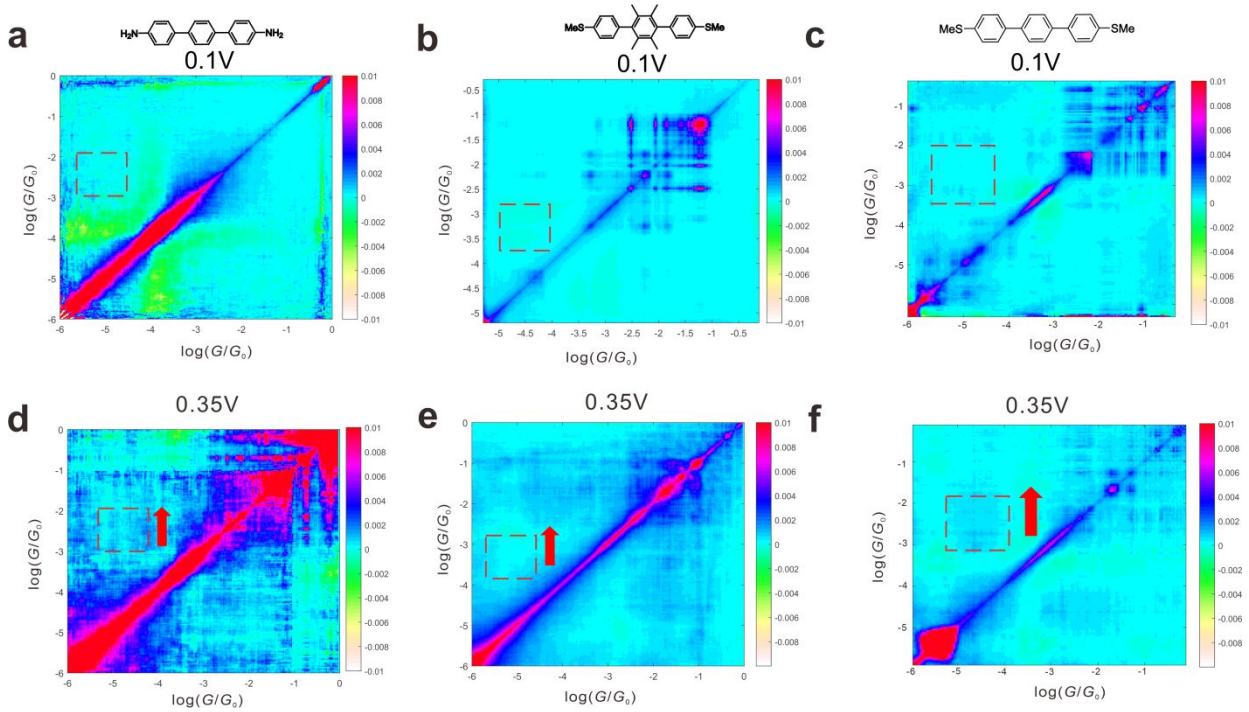


**Figure S19**. Correlation histogram of conductance under a different biases voltage. a-c, the 2D correlation histogram of **N1**, **S1**, and **S3** under 0.10 V. d-f, the 2D correlation histogram of **N1**, **S1,** and **S3** under 0.35 V. The red arrow shows the increase of correlation coefficient under high biases voltage.

## Section 3. Mathematical models of data analysis

1. Flicker noise analysis

First, we transfer the suspending traces into frequency domain signals through the Fast Fourier transform (FFT) method. FFT is an efficient and fast method to transform the time domain signal into the frequency domain signal. The basic idea of FFT is to decompose the original sequence of $N$ points into a series of short sequences for calculation.

The transformation of the aperiodic continuous-time signal $x(t)$ into the frequency domain signal can be expressed as:

$$X(\omega) = \int_{-\infty}^{\infty} x(t) e^{-j\omega t} dt$$

Where $X(\omega)$ is a frequency domain signal. $x(t)$ is a time domain signal.

The expression above is a continuous spectrum of signal $x(t)$. However, what can be obtained in the actual control system is the discrete sampling value $x$(nT) of the continuous signal $x(t)$. Therefore, we need to use the discrete signal $x$(nT) to calculate the spectrum of the signal $x(t)$:

$X(\omega) = \sum_{n=0}^{N-1} x(t) W_N^{kn}$, $k = 0,1, \ldots, N\text{-}1$ where $W$ is a coefficient: $W_N^{kn} = e^{-j\frac{2\pi nk}{N}}$.

Next, the discrete signal is decomposed. The discrete sequence is divided into an odd sequence and even sequence:

$$X(k) = \sum_{n=0}^{N/2-1} x_1(n) W_N^{2kn} + \sum_{n=0}^{N/2-1} x_2(n) W_N^{k(2n+1)}$$

$x_1(n)$ is even sequence, $x_2(n)$ is odd sequence.

Given $W_N^{2kn} = e^{-j\frac{2\pi}{N}2kn} = e^{-j\frac{2\pi}{N/2}kn} = W_N^{kn}$, we get:

$$X(k) = \sum_{n=0}^{N/2-1} x_1(n) W_N^{2kn} + \sum_{n=0}^{N/2-1} x_2(n) W_N^{k(2n+1)}$$

$$= \sum_{n=0}^{N/2-1} x_1(n) W_N^{kn} + W_N^k \sum_{n=0}^{N/2-1} x_2(n) W_N^{kn} = X_1(k) + W_N^k X_2(k)$$

Where $X_1(k)$ and $X_2(k)$ are the DFT of $n/2$ points of $X_1(n)$ and $X_2(n)$, which can be further decomposed, since $X_1(k)$ and $X_2(k)$ both take $N/2$ as the period, $X(k)$ can be expressed as:

$$X(k) = X_1(k) + W_N^k X_2(k)$$

$$X(k + \frac{N}{2}) = X_1(k) - W_N^k X_2(k)$$

After $N$-1 times of decomposition, the Fourier transform of $N$ points is decomposed into $N$ two-point Fourier transforms.

We cut out the conductance-time traces between $10^{-3.0}$ $G_0$ to $10^{-5.0}$ $G_0$ for noise analysis. We used fast Fourier transform to transform the conductance-time signal into a frequency spectrum, and set the sampling point as 4096 ($2^{12}$) to get the noise spectrum of each traces.

Then, we computed the noise power by integrating the gentle signal on the noise spectrum range from 100 Hz to 1000 Hz to separation flicker noise, then normalized the noise by divide the conductance. We also calculated the average conductance of each traces. Thus, we got two eigenvalues

to distinguish each trace and plotted the two-dimensional histogram of normalized flicker noise power and average conductance.

Finally, we fitted the 2D histogram to investigate the charge through of Terphenyl system. We did 2D Gaussian surface fitting and changed the exponent of flick noise power to minimize the correlation between noise and conductance on the 2D histogram of normalized flicker noise power and average conductance. Thus, we counld separate the noise caused by molecular transport and judged the mode of molecular transport. The equation of 2D Gaussian surface fitting are as follows:

$$f(x,y) = Ae^{[-\frac{(x-x_0)^2}{2\sigma_x^2} - \frac{(y-y_0)^2}{2\sigma_y^2}]}$$

We used conjugate gradient methods in Matlab curve fitting toolbox to get the parameters of Gaussian distribution and fit the 2D histogram of normalized flicker noise power and average conductance.

The noise power is proportional to $G^n$ where n is the scaling exponent. To further analysis of transport mode, we studied the relationship between conductance and noise power by fitting the scaling exponent of flicker noise in molecular junctions. The equation of 2D Gaussian can expand as follows:

$$f(x,y) = Ae^{ax^2 + bxy + cx + dy + ey^2 + f}$$

The parameter b represents the correlation between the two variables x and y. We set y as the noise power, and x is the scaling n of $G$. $N$ varies from 1 to 2 in the step of 0.1 when b is close to zero, the corresponding n is the scaling exponent of flicker noise, which get the zeros correlation between $G$ and noise power. Here, we intercepted the region of [$10^{-4.5}$ $G_0$, $10^{-5.5}$ $G_0$] for noise analysis, which make sure that the dimer has enough space to form between the electrodes.
The steps of flicker noise analysis are shown in Figure S20.

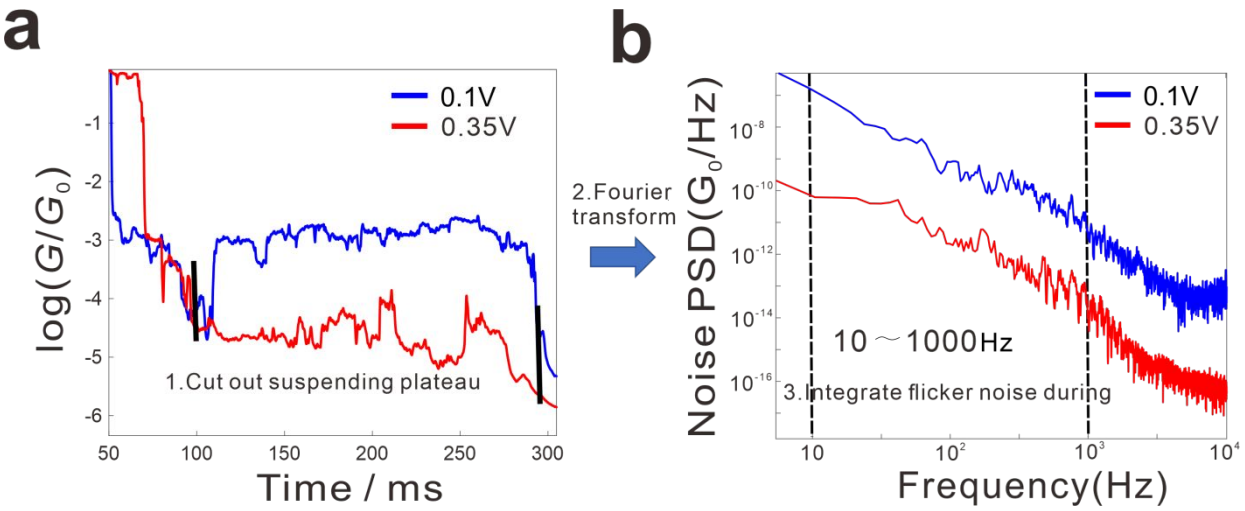


**Figure S20**. The steps for flicker noise calculation. a, Two typically suspended conductance traces of **S1** under different bias, the blue trace is under 0.10 V, the red trace is under 0.35 V. b, The noise spectrum of traces in a, showing the frequency region to integrate flicker noise.

2. Numerical simulation

According to the transmission function, the model of stacking junction is as follows:

$$T(E) = \frac{\Gamma_L \Gamma_R \delta^2}{((E - E_{Frontier})^2 + T_L T_R)^2}$$

Where, $\Gamma_L$ and $\Gamma_R$ are the coupling strength of electrodes and molecules, respectively. $\delta$ is the inter molecule coupling strength.

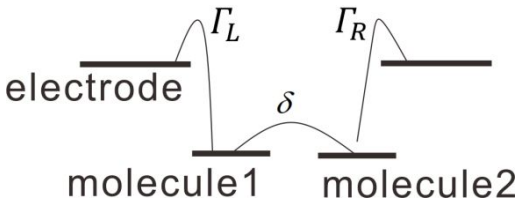


**Figure S21**. The schematic of stacking model.

when $\boldsymbol{E_{Frontier} \gg \Gamma_L \Gamma_R}$. the conductance can be estimated as the following equation according to the transmission function:[7]

$$G = G_0 \frac{\Gamma_L \Gamma_R \sigma^2}{(E - E_{Frontier})^4}$$

We simulated conductance traces by adding the fluctuations described by coupling parameters: $\Gamma$ and $\delta$.

We assumed these fluctuations obey the lognormal distribution as follows:

$$f(\Gamma) = \frac{1}{\Gamma\sigma\sqrt{2\pi}} e^{\frac{(log(\Gamma))^2}{-2\sigma^2}}$$

Thus, noise from intramolecular transport is mainly between the electrode and the molecule, which is described by white noise with the variance of $\Gamma$ obey lognormal distribution. For intermolecular transport, we add another log(normal) noise $\delta$ from each simulated traces.

For monomer junction, we only introduced intramolecular noise $\Gamma$. The variation of the noise added on each traces obey the lognormal distribution, which is decided by:

$$\Gamma = \frac{\Gamma_{noise} \sigma_{Bond}}{\Gamma_{Bond,0}}$$

Where, $\Gamma_{noise}$ is the energy of the intramolecular coupling strength. $\sigma_{Bond}$ is the standard deviation of through-bond coupling distinguish from intermolecular through-space transport. $\Gamma_{(Bond,0)}$ is a compensation coefficient to ensure the fluctuation of $\sigma$ is on the same scale as fluctuations of $\Gamma$. Here, we set the values: $\sigma_{Bond}$=0.4, $\Gamma_{noise}$=100 meV, $\Gamma_{(Bond,0)}$=150 meV.

For stacking junction, we introduced another intermolecular noise $\delta$ for each simulating traces to simulate the overall deviation of each single conductance trace from a stronger coupling strength from through space transport through the equation:

$$\delta = \frac{\delta_{noise} \sigma_{space}}{\Gamma_{Bond,0}}$$

with the values that $\sigma_{space}$=0.6, $\delta_{noise}$=150 meV, $\Gamma_{(Bond,0)}$=150 meV.

Using Monte Carlo simulation, we generated 30000 conductance traces for the monomer and stacking junction respectively and drawed a flicker noise distribution histogram between noise power versus average conductance. We found intermolecular stronger noise brings greater noise and conductance variation to bring more through-space transport.

3. Feature traces extraction

We defined the 'twist' and 'stacking' trajectory characteristics to investigate the dynamic process of stacking.[2, 8] We set a sliding box with a length of 0.1 nm to scan each conductance data points on the traces. During a sliding process, if the slope (absolute value) in the box is more than N times than the two boxes before and after it with a positive or negative value, the traces are considered to have the characteristics of 'twist' or 'stacking'. Thus, the rapid decrease or rise of the conductance between the conductance plateaus is defined by the slope (Figure S22). The evaluation criteria can be expressed by the following formula:

$$N|k_R| \leq \pm\, k$$
$$N|k_L| \leq \pm\, k$$
$$k\ < 0$$

Where, $k$=$\Delta G_n/\Delta L$ , $N$=2, the pre-k sign is positive for a twist with $\Delta L$=0.05 nm and negative for stacking with $\Delta L$=0.1 nm.

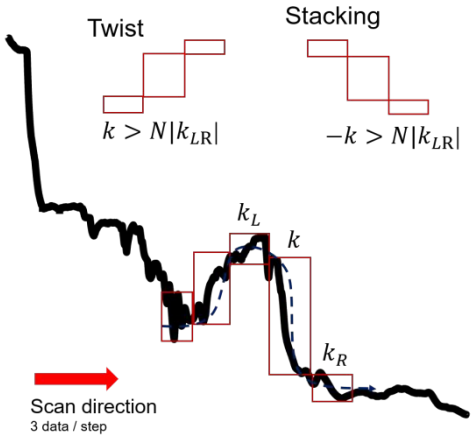


**Figure S22.** The schematic diagram of judging traces features.

Then we draw the 2D histogram by these selected traces. The points according to conductance increase will be recorded, which is defined as the middle point of the center box. The traces with conductance increase will be aligned by these points to get a clear trend of conductance jump.

4. The range of conductance jump

We designed an algorithm for scanning the traces with stable conductance jump and counting the range of conductance change in these traces, which was used in Figure 5f. We selected the traces with 'twist' feature. Then, the traces with conductance increase more than $10^{0.2}$ $G_0$ conductance with a conductance plateaus more than 0.02 nm before and after the jumping point was recorded. The maximum conductance difference between the two plateaus is used as the range of conductance increases. We drew a 1D histogram to compare the range distribution of different molecules.

5. Conductance plateaus scan and counting

We counted the plateau when suspending the tips for 200 ms, and calculated the average conductance of each plateau. We used a 10 ms sliding box and calculated the slope of each box to ensure that it terminates at the end of the plateau, and scanned the next plateau. The following is the schematic diagram of the plateau statistical process.

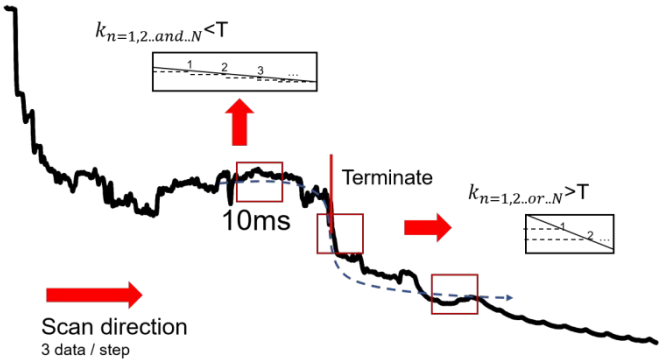


**Figure S23**. The schematic diagram of counting the plateaus.

6. Correlation analysis

To study the sequence of each conductance state, we constructed the correlation histogram of a sliding square window. The trace is divided into a sliding square window with a length of 0.1 nm. The correlation coefficients value p through the Pearson correlation between the previous window and the subsequent window is calculated. The average conductance of the two windows that are positively correlated with a value more than the threshold value 0.1 will be calculated. Take the conductance of the first window as the X-axis, and the conductance of the second window as the Y-axis to draw a two-dimensional conductance correlation histogram through distance windows. Thus, we can get the order of plateaus to appear to show a stacking process of [$10^{-3.0}$ $G_0$, $10^{-5.0}$ $G_0$] region. The Figure S24 shown the steps of this method is as follows:

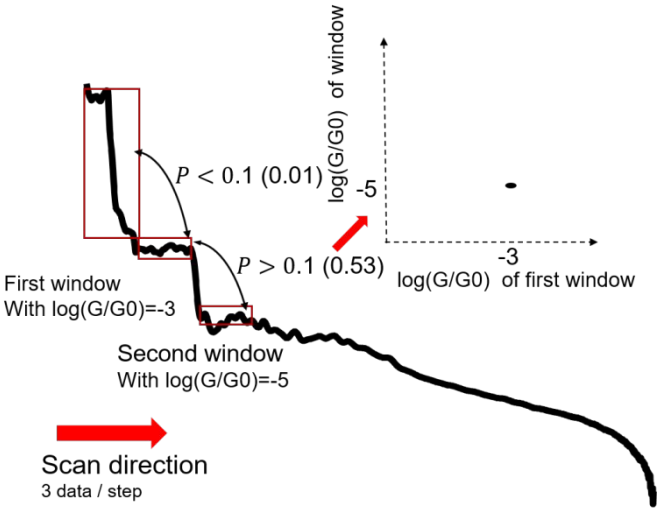


**Figure S24**. The schematic diagram of correlation analysis through distance.

7. Conductance noise analysis

We analyzed all collected break-junction traces of **S1** and calculated the conductance noise as follows. First, we select the conductance range to analyze. The ranges are between [-3, -4] and [-4.5, -5.5] log($G/G_0$), respectively, for the conductance from monomer and dimers according to theoretical

calculation. Then, we choose the traces with a long plateau in the range above that formed a molecular junction to analyze the conductance noise of two ranges (above 0.5 times of the average plateau length). Next, we use a smoothed reference trace to reduce the conductance sequences during the range of conductance plateaus. This reference trace is obtained by low-pass filtering of the raw data. The filtering method is 'smooth', and the span *N* is window width, set as 100. We subtract the smoothed reference traces from the raw conductance range to obtain the normalized traces. Finally, we calculate the standard deviation of the normalized sequence as conductance noise to evaluate the fluctuation of the specific range of break-junction traces.

## Section 4. Theoretical calculations

All the geometry optimizations and frequency analysis of the molecules were carried out using Gaussian 16.[9] The B3LYP-D3(BJ) functional[10-12] together with 6-31G(d) basis set[13] was used for geometry optimization in the gas phase. Frequency analysis was conducted at the same level of theory to verify that the stationary points are minima or transition states. The single point energies were then calculated using the M06-2X functional,[14] and 6-311+G(d,p) basis set with the SMD solvation model.[15] 1,2,4-trichlorobenzene was used as the solvent. Since 1,2,4-trichlorobenzene are not available in Gaussian 16, the parameters of chlorobenzene were used. As shown in Figure S25, the direction of the electric field in the optimization of stacking dimer is along the molecular skeleton (from atom S1 to atom S2), which is consistent with the direction adopted in the optimization of monomer structure. Based on the optimized dimer structures, we applied the electric field directions from atom S1 to atom S2 and from atom S1 to atom S3 respectively to calculate the single point energy.

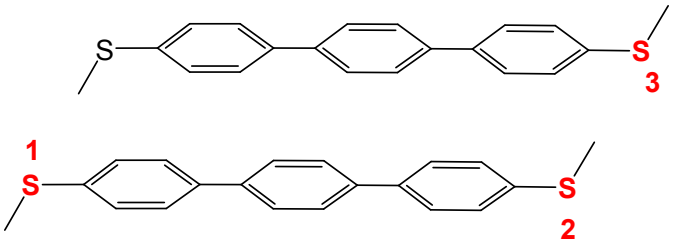


**Figure S25**. The stacking model of **S1**.

The geometry optimization and transmission functions of the single-molecule device were calculated using GGA and PBE functional with the NEGF approach in Atomistix Tool Kit (ATK) package.[16-18] To construct the single-molecule device models, the molecule structures were optimized by Gaussian 16, as described above. Then, each target molecule was attached to the gold atoms at two gold electrodes to fabricate the typical gold-molecule-gold model. When the device configurations were optimized with the ATK package, the molecules in the center of the device were rigid and just optimized the coupling with the electrode. The single-ζ polarized (SZP) basis set was used for Au atoms and the double-ζ polarized (DZP) basis set were used for other atoms, with a real-space grid defined with an equivalent energy cut-off of 75 Hartree, while the k-points of 3, 3, 134 were used for geometry optimization and 7, 7 for transmission functions.

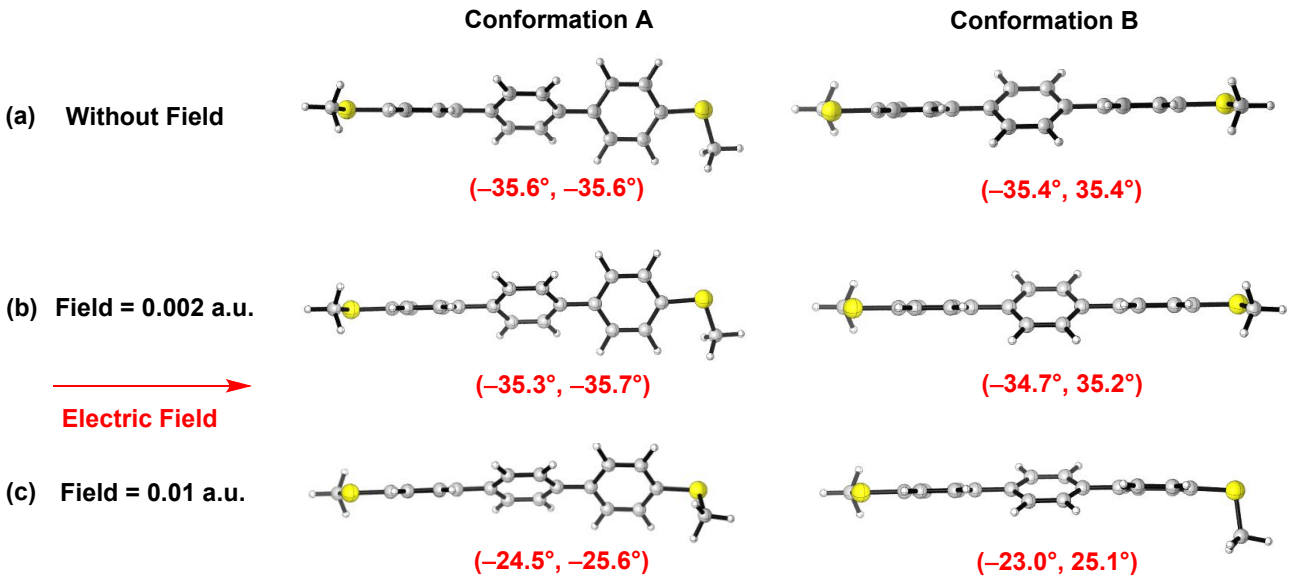


**Figure S26**. The optimized structures of **S1**. The optimized structures of **S1** (a) in the absence of the field, (b) with a field of 0.002 a.u., and (c) with a field of 0.01 a.u.. The direction of the electric field is along the two sulfur atoms anchored with the electrodes, and the dihedral angles between adjacent benzene rings in **S1** are given below the structures (in red).

As shown in Figure S26a, the calculations indicated there are two stable conformations (A and B) in the rotation of the C-C bond between the adjacent benzene rings of **S1**, and without a considerable difference in energy. In the absence of an electric field, the dihedral angles between the adjacent benzene rings in both conformations are about 35°, which makes it difficult to form the stacking dimer. When a field of 0.002 a.u. (1.03 V/nm) is applied, the dihedral angles between the adjacent benzene rings in both conformations remain almost unchanged (Figure S26b). As the external field increases to 0.01 a.u. (5.14 V/nm), the dihedral angles between the adjacent benzene rings in both conformations decrease to about 25° (Figure S26c), which means the π electrons become more delocalized and the formation of stacking dimer becomes more favorable. Here, only the stacking configuration of conformation B was considered under the electric field because the coplanarity of the phenyl rings on both sides of the **S1** favors the formation of intermolecular stacking.

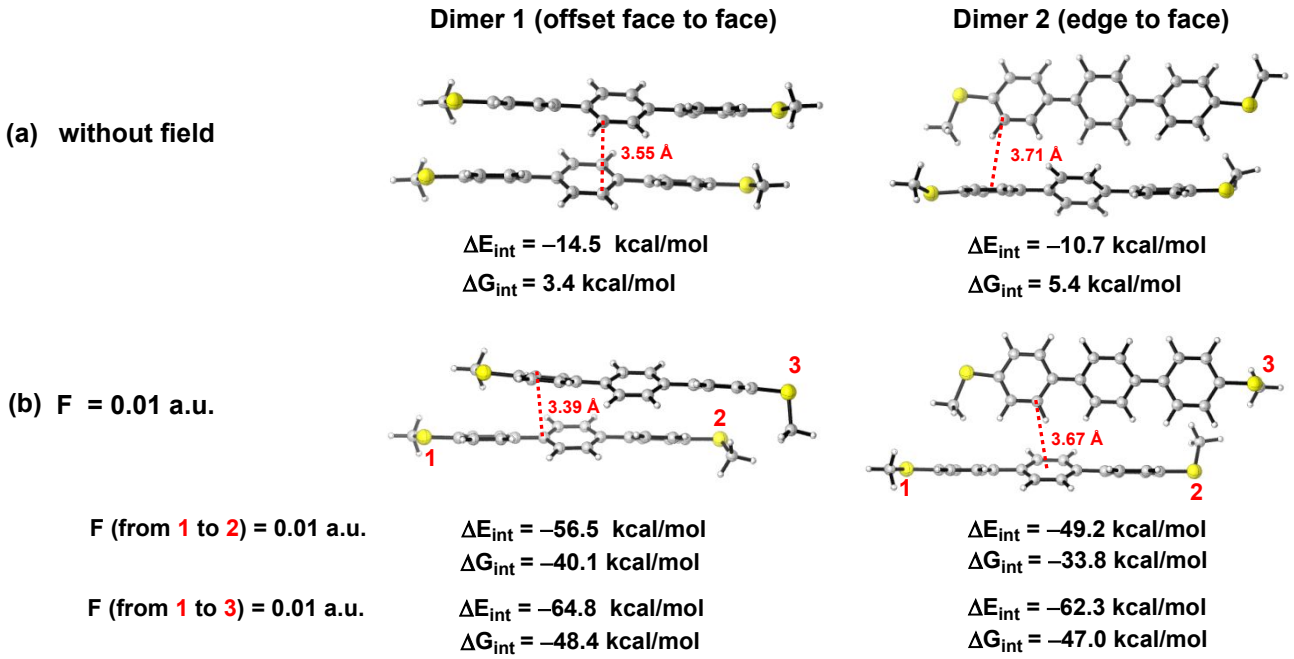

**Figure S27**. The optimized structures and interaction energies of the dimers of **S1**. The optimized structures and interaction energies of dimers (a) without the electric field and (b) with the electric field of 0.01 a.u. with different directions, from atom 1 to atom 2 and from atom 1 to atom 3, respectively. The interaction energies are given below each structure and calculated using M06-2X/6-311+G(d,p)/SMD(chlorobenzene)//B3LYP-D3(BJ)/6-31G(d).

There should be two optimal ways of stacking in this system, which are offset face to face stacking and edge to face stacking, respectively.[19] As shown in Figure S27, the energy comparison of these two configurations was carried out, and dimer 1 represents the offset face to face stacking, while dimer 2 represents the edge to face stacking. As shown in Figure S27a, the distance of π-π between two monomers in dimer 1 is measured by the distance between the vertically opposed C atoms, while the distance of C-H---π between two monomers in dimer 2 is measured by the distance from the C atom to the center of the benzene ring (red dash line in Figure S27). The initial distance in dimer 1 is controlled at about 3.70 Å, while the initial distance in dimer 2 is controlled at about 3.8 Å. Since the most suitable distance for the benzene stacking is considered to be about 3 ~ 4 Å,[20-21] considering the hindrance of terphenyl due to the non-coplanarity, the initial distance we choose is considered to be appropriate. Then the dimers were optimized to the minima. The distance in the minima of dimer 1 is 3.55 Å, and the distance in the minima of dimer 2 is 3.71 Å. The optimal configuration under no electric field is used as the initial structure, and the optimization of the dimer configuration under an electric field is carried out using the same theoretical level. The effect of the electric field is studied using the "Field = M ± N" keyword in Gaussian 16. With the electric field of 0.01 a.u. directed from atom 1 to atom 2, as shown in Figure S27b, the distance in the minima of dimer 1 is 3.39 Å, and the distance in the minima of dimer 2 is 3.67 Å.

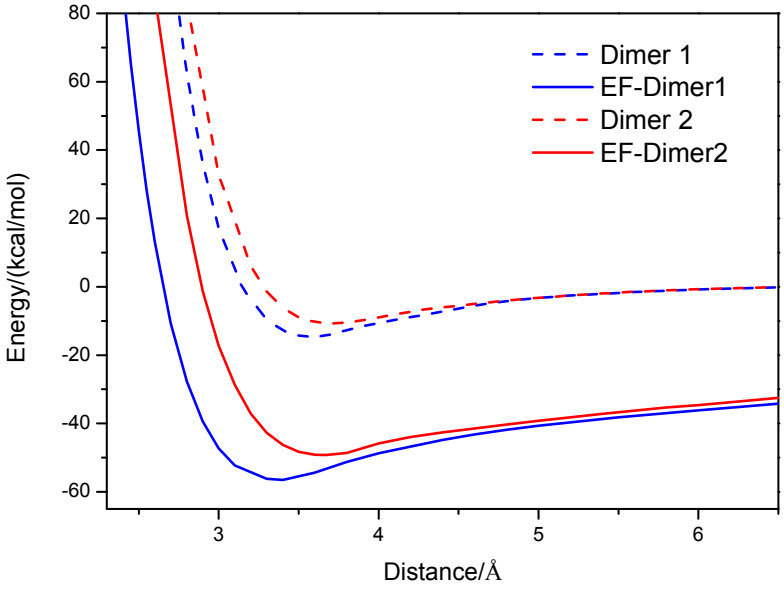


**Figure S28**. Vertical separation profiles for the dimers of **S1**. Vertical separation profiles for dimer 1 (offset face to face) in blue and dimer 2 (edge to face) in red, without field (dotted line) and with a field of 0.01 a.u. from atom 1 to atom 2 (solid line), respectively, and calculated using M06-2X/6-311+G(d,p)/SMD(chlorobenzene).

We also calculated the vertical separation profiles for dimers of **S1**, as shown in Figure S28, and the definition of the distance is consistent with Figure S27. It should be noted that the energy of the monomer will reduce under the electric field, so when we calculate the interaction energy under the electric field, we use the energy of the dimer under the electric field to subtract the energy of the two

monomers under the electric field. That is to say, the ordinate zero of the dotted line and the solid line in Figure S28 represent different meanings, which are the energy of the two monomers without the electric field and the energy of the two monomers under the electric field, respectively. Without the electric field, the distance between the monomers in the energy minima of dimer 1 is 3.55 Å, and the distance in the energy minima of dimer 2 is 3.71 Å. With an electric field of 0.01 a.u. from atom 1 to atom 2, the distance between the monomers in the minima of dimer 1 changes to 3.39 Å, and the distance in the minima of dimer 2 changes to 3.67 Å. The interaction of stacking under the electric field is more long-range, and we attribute it to the significant increase in the induced dipole moment under the electric field.

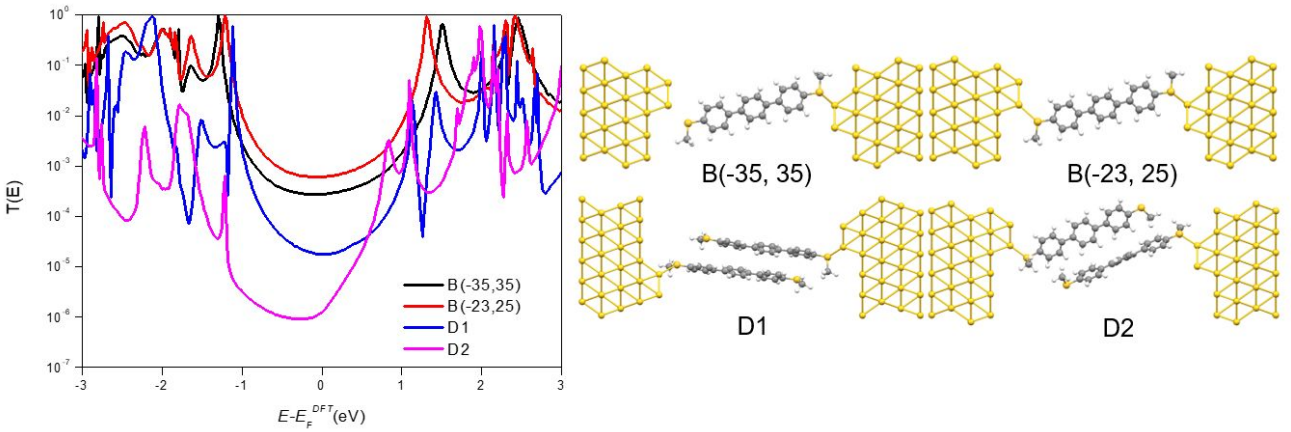


**Figure S29**. Structure diagrams and transmission curves of the devices. The zero-bias transmission curves of the conformation B with the different twisted angle between adjacent benzene rings are calculated, which are represented by B (-35, 35) (black) and B (-23, 25) (red), respectively. The zero-bias transmission curves of the stacking dimers, which are represented by **D1** (offset face to face, blue) and **D2** (edge to face, pink).

The investigations of Venkataraman *et al.*[22] showed that the conductance for the biphenyl decreases with increasing twist angle and satisfy the cosine-squared relation. Thus, the conductance of conformation A and B are considered to be equal since the dihedral angles between the adjacent benzene rings in both conformations are almost the same. We only calculate the transmission curves of conformation B. As shown in Figure S29, the zero-bias transmission curves of B (-35, 35), B (-23, 25), and the stacking dimers were calculated using ATK package. Compared with the monomer, the transmission of the dimer is much lower. Since **D1** (offset face to face) is thermodynamically much more favorable compared with **D2** (edge to face), and the conductance of **D2** may overlap with the background, dimers detected in the experiments are considered to be **D1**. The calculated transmission is consistent with the experimental conductance.

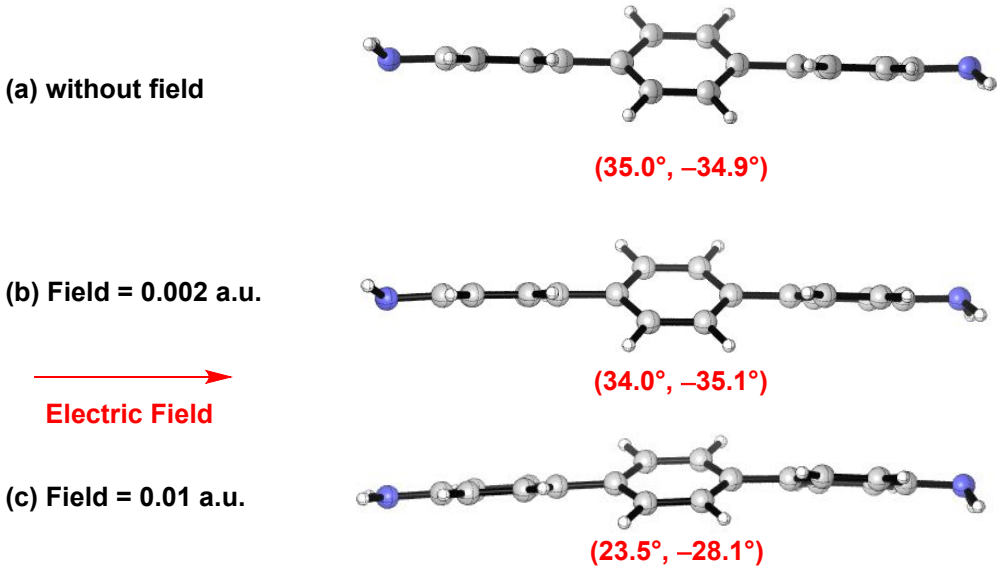


**Figure S30**. The optimized structures of **N1**. The optimized structures of **N1** (a) in the absence of electric field, (b) with the field of 0.002 a.u., and (c) with the field of 0.01 a.u.. The direction of the electric field is along two N atoms.

The strong electric field along the two sulfur atoms of **S1** destroys the electron-donating effect of the p-π conjugation of the S atom on the right side of the **S1** because the direction of the electron transfer is opposite to the direction of the electric field. Thus, as shown in Figure S26c, under the electric field of 0.01 a.u., due to the destruction of p-π conjugation, the steric effect dominates the conformation of the right SMe of **S1**. Because of the steric hindrance of the methyl group, the SMe group will turn to the direction perpendicular to the plane of the benzene ring. The coupling between **S1** and the gold electrode will limit this deformation process and prevents the dihedral angle of the molecule from decreasing. Besides, the vertically-oriented SMe would cause steric hindrance during the stacking process.

As shown in Figure S30c, under an electric field, since the electric field promotes the electron transfer from the N atom to the benzene ring, the p-π conjugation of the N atom on the left of **N1** is enhanced, and the N atom tends to $sp^2$ hybridized, and $NH_2$ tends to coplanar with the adjacent benzene ring. While for the N atom on the right of **N1**, the p-π conjugation would be destroyed, because the direction of the electron transfer is opposite to the direction of the electric field, and the dihedral angle between $NH_2$ and benzene ring increases.[23] Compared with **S1**, the orientation of the lone pair of electrons on the N atom of **N1** is almost unchanged after the molecular deformation under an electric field of 0.01 a.u., so the coupling between **N1** and the gold electrode will not impede the molecular deformation.

Thus, **N1** exhibits a higher ratio of 'twist' and 'stacking' traces than **S1**, especially at higher bias voltage.

**References**


1. Chen, Z.; Chen, L.; Liu, J.; Li, R.; Tang, C.; Hua, Y.; Chen, L.; Shi, J.; Yang, Y.; Liu, J.; Zheng, J.; Chen, L.; Cao, J.; Chen, H.; Xia, H.; Hong, W., Modularized Tuning of Charge Transport through Highly Twisted and Localized Single-Molecule Junctions. *J. Phys. Chem. Lett.* **2019**, *10*, 3453-3458.
2. Jiang, F.; Trupp, D. I.; Algethami, N.; Zheng, H.; He, W.; Alqorashi, A.; Zhu, C.; Tang, C.; Li, R.; Liu, J.; Sadeghi, H.; Shi, J.; Davidson, R.; Korb, M.; Sobolev, A. N.; Naher, M.; Sangtarash, S.; Low, P. J.; Hong, W.; Lambert, C. J., Turning the Tap: Conformational Control of Quantum Interference to Modulate Single-Molecule Conductance. *Angew. Chem., Int. Ed.* **2019**, *58*, 18987-18993.
3. Zang, Y.; Stone, I.; Inkpen, M. S.; Ng, F.; Lambert, T. H.; Nuckolls, C.; Steigerwald, M. L.; Roy, X.; Venkataraman, L., In Situ Coupling of Single Molecules Driven by Gold - Catalyzed Electrooxidation. *Angew. Chem., Int. Ed.* **2019**, *58*, 16008-16012.
4. Aradhya, S. V.; Frei, M.; Hybertsen, M. S.; Venkataraman, L., Van der Waals interactions at metal/organic interfaces at the single-molecule level. *Nat. Mater.* **2012**, *11*, 872-876.
5. Frisenda, R.; Janssen, V. A.; Grozema, F. C.; van der Zant, H. S.; Renaud, N., Mechanically controlled quantum interference in individual pi-stacked dimers. *Nat. Chem.* **2016**, *8*, 1099-1104.
6. Inkpen, M. S.; Liu, Z. F.; Li, H.; Campos, L. M.; Neaton, J. B.; Venkataraman, L., Non-chemisorbed gold-sulfur binding prevails in self-assembled monolayers. *Nat. Chem.* **2019**, *11*, 351-358.
7. Magyarkuti, A.; Adak, O.; Halbritter, A.; Venkataraman, L., Electronic and mechanical characteristics of stacked dimer molecular junctions. *Nanoscale* **2018**, *10*, 3362-3368.
8. Herrer, I. L.; Ismael, A. K.; Milan, D. C.; Vezzoli, A.; Martin, S.; Gonzalez-Orive, A.; Grace, I.; Lambert, C.; Serrano, J. L.; Nichols, R. J.; Cea, P., Unconventional Single-Molecule Conductance Behavior for a New Heterocyclic Anchoring Group: Pyrazolyl. *J. Phys. Chem. Lett.* **2018**, *9*, 5364-5372.
9. Frisch, M.; Trucks, G.; Schlegel, H.; Scuseria, G.; Robb, M.; Cheeseman, J.; Scalmani, G.; Barone, V.; Petersson, G.; Nakatsuji, H., Gaussian 16. In *Revision A*, Gaussian, Inc., Wallingford CT: 2016.
10. Ehrlich, S.; Moellmann, J.; Grimme, S., Dispersion-Corrected Density Functional Theory for Aromatic Interactions in Complex Systems. *Acc. Chem. Res.* **2013**, *46*, 916-926.
11. Becke, A. D., Density-functional thermochemistry. III. The role of exact exchange. *J. Chem. Phys.* **1993**, *98*, 5648-5652.
12. Zhao, Y.; Truhlar, D. G., A new local density functional for main-group thermochemistry, transition metal bonding, thermochemical kinetics, and noncovalent interactions. *J. Chem. Phys.* **2006**, *125*, 194101.
13. Hariharan, P. C. P.; Pople, J. A., The Influence of Polarization Functions on Molecular Orbital Hydrogenation Energies. *Theor. Chim. Acta.* **1973**, *28*, 213-222.
14. Zhao, Y.; Schultz, N. E.; Truhlar, D. G., Exchange-correlation functional with broad accuracy for metallic and nonmetallic compounds, kinetics, and noncovalent interactions. *J. Chem. Phys.* **2005**, *123*, 161103.
15. Marenich, A. V.; Cramer, C. J.; Truhlar, D. G., Universal Solvation Model Based on Solute Electron Density and on a Continuum Model of the Solvent Defined by the Bulk Dielectric Constant and Atomic Surface Tensions. *J. Phys. Chem. B* **2009**, *113*, 6378-6396.

16. Perdew, J. P.; Burke, K.; Ernzerhof, M., Generalized Gradient Approximation Made Simple. *Phys. Rev. Lett.* **1996**, *77*, 3865-3868.
17. Brandbyge, M.; Mozos, J. L.; Ordejón, P.; Taylor, J.; Stokbro, K., Density functional method for nonequilibrium electron transport. *Phys. Rev. B* **2002**, *65*, 165401.
18. Soler, J. M., The SIESTA method for ab initio order-N materials simulation. *J. Phys. Condens. Matter* **2002**, *14*, 2745-2779.
19. Neel, A. J.; Hilton, M. J.; Sigman, M. S.; Toste, F. D., Exploiting non-covalent pi interactions for catalyst design. *Nature* **2017**, *543*, 637-646.
20. Tsuzuki, S.; Honda, K.; Uchimaru, T.; Mikami, M.; Tanabe, K., Origin of Attraction and Directionality of the π/π Interaction: Model Chemistry Calculations of Benzene Dimer Interaction. *J. Am. Chem. Soc.* **2002**, *124*, 104-112.
21. Hutchison, G. R.; Ratner, M. A.; Marks, T. J., Intermolecular Charge Transfer between Heterocyclic Oligomers. Effects of Heteroatom and Molecular Packing on Hopping Transport in Organic Semiconductors. *J. Am. Chem. Soc.* **2005**, *127*, 16866-16881.
22. Venkataraman, L.; Klare, J. E.; Nuckolls, C.; Hybertsen, M. S.; Steigerwald, M. L., Dependence of single-molecule junction conductance on molecular conformation. *Nature* **2006**, *442*, 904-907.
23. Tao, S.; Yu, L.-J.; Pang, R.; Huang, Y.-F.; Wu, D.-Y.; Tian, Z.-Q., Binding Interaction and Raman Spectra of p−π Conjugated Molecules Containing CH2/NH2Groups Adsorbed on Silver Surfaces: A DFT Study of Wagging Modes. *J. Phys. Chem. C* **2013**, *117*, 18891-18903.